NANO LETTERS

Subscriber access provided by Bethel University

Communication

Multi-wavelength Single Nanowire InGaAs/ InP Quantum Well Light Emitting Diodes

Inseok Yang, Ziyuan Li, Jennifer Wong-Leung, Yi Zhu, Zhe Li, Nikita Gagrani, Li Li, Mark N. Lockrey, Hieu Nguyen, Yuerui Lu, Hark Hoe Tan, Chennupati Jagadish, and Lan Fu

Nano Lett., **Just Accepted Manuscript** • DOI: 10.1021/acs.nanolett.9b00959 • Publication Date (Web): 29 May 2019

Downloaded from http://pubs.acs.org on May 30, 2019

Just Accepted

"Just Accepted" manuscripts have been peer-reviewed and accepted for publication. They are posted online prior to technical editing, formatting for publication and author proofing. The American Chemical Society provides "Just Accepted" as a service to the research community to expedite the dissemination of scientific material as soon as possible after acceptance. "Just Accepted" manuscripts appear in full in PDF format accompanied by an HTML abstract. "Just Accepted" manuscripts have been fully peer reviewed, but should not be considered the official version of record. They are citable by the Digital Object Identifier (DOI®). "Just Accepted" is an optional service offered to authors. Therefore, the "Just Accepted" Web site may not include all articles that will be published in the journal. After a manuscript is technically edited and formatted, it will be removed from the "Just Accepted" Web site and published as an ASAP article. Note that technical editing may introduce minor changes to the manuscript text and/or graphics which could affect content, and all legal disclaimers and ethical guidelines that apply to the journal pertain. ACS cannot be held responsible for errors or consequences arising from the use of information contained in these "Just Accepted" manuscripts.

is published by the American Chemical Society. 1155 Sixteenth Street N.W., Washington, DC 20036
Published by American Chemical Society. Copyright © American Chemical Society. However, no copyright claim is made to original U.S. Government works, or works produced by employees of any Commonwealth realm Crown government in the course of their duties.

1
2
3
4
5
6
7
8
9
10
11
12
13
14
15
16
17
18
19
20
21
22
23
24
25
26
27
28
29
30
31
32
33
34
35
36
37
38
39
40
41
42
43
44
45
46
47
48
49
50
51
52
53
54
55
56
57
58
59
60

Multi-wavelength Single Nanowire InGaAs/InP Quantum Well Light Emitting Diodes

Inseok Yang[1], Ziyuan Li[1], Jennifer Wong-Leung[1], Yi Zhu[1,2], Zhe Li[3], Nikita Gagrani[1], Li Li[4], Mark N. Lockrey[4], Hieu Nguyen[2], Yuerui Lu[2], Hark Hoe Tan[1], Chennupati Jagadish[1] and Lan Fu[1]**

1 Department of Electronic Materials Engineering, Research School of Physics and Engineering, The Australian National University, Canberra, ACT 2601, Australia

2 Research School of Electrical, Energy and Materials Engineering, The Australian National University, Canberra, ACT 2601, Australia

3 Department of Applied Mathematics, Research School of Physics and Engineering, The Australian National University, Canberra, ACT 2601, Australia

4 Australian National Fabrication Facility, Research School of Physics and Engineering, The Australian National University, Canberra, ACT 2601, Australia

Corresponding Author

*Email: inseok.yang@anu.edu.au

*Email: lan.fu@anu.edu.au

KEYWORDS: selective area epitaxy; MOCVD; nanowires; InGaAs/InP quantum wells; single nanowire LEDs;

ABSTRACT: We report multi-wavelength single InGaAs/InP quantum well nanowire light emitting diodes grown by metal organic chemical vapor deposition using selective area epitaxy technique and reveal the complex origins of their electroluminescence properties. We observe that the single InGaAs/InP quantum well embedded in the nanowire consists of three components with different chemical compositions, axial quantum well, ring quantum well and radial quantum well respectively, leading to the electroluminescence

emission with multiple wavelengths. The electroluminescence measurements show a strong dependence on current injection levels as well as temperatures and these are explained by interpreting the equivalent circuits in a minimized area of the device. It is also found that the electroluminescence properties are closely related to the distinctive triangular morphology with an inclined facet of the quantum well nanowire. Our study provides important new insights for further design, growth and fabrication of high performance quantum well-based nanowire light sources for a wide range of future optoelectronic and photonic applications.

Integrated photonics has drawn tremendous attention as the key technology to realize high bandwidth communications[1] for on-chip big data processing to fulfil important requirements for artificial intelligence,[2] fifth generation (5G) wireless communications[3] and so on. To achieve low power consumption and highly compact photonic integrated circuits (PICs), monolithically integrated electrically injected nanoscale light sources are essential. Currently, silicon (Si) is the most commonly used substrate for PICs due to its cost

effectiveness and advanced processing technologies matured for decades.[4] However, it is challenging for Si itself to be employed as a light source[5] due to its indirect bandgap. On the other hand, III-V compound semiconductors can be good alternatives thanks to their direct bandgap and thus superior light emitting properties.[6] Importantly, by employing one-dimensional nanowire (NW) structures, it is promising to epitaxially grow high quality III-V semiconductor materials on lattice mismatched substrates such as Si owing to their effective lateral strain relaxation.[7, 8] Among various techniques for NW synthesis,[9] the catalyst-free selective area epitaxy (SAE), has distinct advantages of high uniformity (in NW size, composition and position), flexibility (in device design), and free from metal contamination issues which may be detrimental to device performances.[10-12] So far, a few SAE grown III-V[13-18] as well as III-nitride-based[19-22] NW light emitting diodes (LEDs) emitting at near-infrared and visible wavelengths have been reported. To achieve a high luminescence efficiency at wavelengths between 1.3 to 1.6 μm for telecommunications application,[23] the growth of InGaAs(P)/InP quantum wells (QWs) is the most common and effective approach.[15, 16, 24-26] Recently, core-shell InGaAs/InP multi-QW (MQW) nanopillar array LEDs on Si by SAE with ~ 1.5 μm vertical emission have been reported.[16] However,

1
2
3
4
5
6
7
8
9
10
11
12
13
14
15
16
17
18
19
20
21
22
23
24
25
26
27
28
29
30
31
32
33
34
35
36
37
38
39
40
41
42
43
44
45
46
47
48
49
50
51
52
53
54
55
56
57
58
59
60

so far, multi-wavelength single NW-based InGaAs(P)/InP QW-NW LEDs in the horizontal direction, which has potential applications as integrated wavelength-selective LEDs for on-chip nanophotonics, have not been demonstrated yet. As shown previously, single horizontal NW devices such as optically pumped lasers,[13, 14, 27-29] LEDs,[30] photodetectors,[31-33] and solar cells[34-36] provided important platform for fundamental understanding of the structural, optical and electrical properties of nanoscale devices and their potential applications. Furthermore, their unique geometry-related light emission and absorption properties may lead to different requirements for device design from vertical NW devices. We also have recently reported the three-dimensional growth mechanisms of InGaAs/InP MQW NWs by SAE,[37] and revealed that the MQW NW's wurtzite (WZ) InP base has a hexagonal column with $\{1\bar{1}00\}$ side facets and truncated $\{\bar{1}102\}$ facets on the top. The subsequent QW has a three-fold symmetric formation on the base. Consequently, the QW thicknesses and compositions on each facet are expected to be different and this may lead to a complex luminescence behavior. Hence, these factors have to be carefully considered in designing related devices such as LEDs, lasers and possible quantum well infrared photodetectors (QWIPs)[38] with SAE grown QW structures.

In this work, we demonstrated multi-wavelength InGaAs/InP QW-NW LEDs grown by metal organic chemical vapor deposition (MOCVD) using SAE technique. From spherical aberration corrected scanning transmission electron microscopy (AC-STEM), it is revealed that the QW consists of three components with different chemical compositions, radial QW, ring QW and axial QW, leading to a multi-wavelength photoluminescence (PL) and electroluminescence (EL) spectra. Furthermore, it is found that the EL spectra of the QW-NW LEDs exhibit a significant dependence on current injection levels as well as measurement temperatures. These properties are closely related to the QW-NW's distinctive triangular and inclined faceted morphology, which can be explained by careful examination of the equivalent circuits of the single NW device. From the Finite-Difference Time-Domain (FDTD) simulation, it is also revealed that the inclined facet affects the optical mode confinement leading to enhanced light extraction efficiency. Furthermore, the emitted light can also be strongly absorbed by the gold contacts, leading to reduced light extraction. Based on above, we propose several design guidelines for realization of highly efficient and functional QW-NW LEDs for future applications.

Experimental Methods

Preparation of Nanowire Growth Template: Prior to NW growth, the SAE growth templates were prepared first. A SiO_2 layer of ~ 30 nm was deposited on a (111)A InP wafer at 300 °C by atomic layer deposition (ALD) followed by mask patterning by electron beam lithography (EBL) in a Raith 150 EBL system. After a wet chemical etching in a solution of 48% hydrofluoric acid diluted in ammonium fluoride with a ratio of 1:45, a final mask pattern consisting of a 200 x 200 μm hexagonal array with a final hole diameter of 150 nm and pitch of 800 nm were fabricated as a template for subsequent SAE growth.

Nanowire Growth Process: The InP (p)-InGaAs/InP QW (i)-InP (n) NW arrays were grown by SAE technique in an AIXTRON 200/4 MOCVD system at a pressure of 100 mbar with H_2 as the carrier gas. Trimethylindium (TMIn) and phosphine (PH_3) were used as precursors for both InP base (p-doped) and top (n-doped) segments. TMIn and trimethylgallium (TMGa) and arsine (AsH_3) were used as precursors for the InGaAs QW. The InP base and top segments were grown at 700 °C for 5 and 8 min, respectively with a V/III ratio of 80.9, TMIn flow rate of 6.07×10^{-6} mol/min and PH_3 flow rate of 4.91×10^{-4}

mol/min. Dimethylzinc of 8.63×10^{-6} mol/min and silane of 3.08×10^{-7} mol/min were used as dopants for p-doped InP based segment and n-doped InP top segment respectively. A single InGaAs QW was grown at 700 °C for 5 s between the InP base and top segments with a V/III ratio of 80.7 by setting TMIn, TMGa and AsH_3 flow rates to 3.37×10^{-6}, 8.80×10^{-6} and 9.82×10^{-4} mol/min respectively. The total flow rate was maintained at 14.5 l/min for all growth segments.

Single nanowire LED fabrication: To fabricate single NW LEDs, first the as-grown NWs were mechanically transferred onto a 300 nm-thick SiO_2 thermally grown on a Si substrate. Subsequently, electrode patterns were defined by EBL at the two ends of the NWs followed by 9% HCl wet etching to remove the native oxide on both p- and n-contacts. The electrical contacts were formed by depositing 10 nm titanium and 220 nm gold by electron beam evaporation followed by a lift-off process. The final device was mounted and wire-bonded to a 16-pin ceramic package (see Figure S1 in Supporting Information for fabrication process images).

Characterization Method: The morphology of NWs was characterized by SEM using a FEI VERIOS 460 system with an accelerating voltage of 5.0 kV and a current of 50 pA.

1
2
3
4
5
6
7
8
9
10
11
12
13
14
15
16
17
18
19
20
21
22
23
24
25
26
27
28
29
30
31
32
33
34
35
36
37
38
39
40
41
42
43
44
45
46
47
48
49
50
51
52
53
54
55
56
57
58
59
60

The microstructure and chemical composition of the QW were analyzed by AC-STEM using a JEOL JEM-ARM200F system equipped with a JEOL Centurio EDX detector. The optical properties of NWs were characterized by CL and μ-PL spectroscopy at room temperature. The CL images were acquired with a FEI VERIOS 460 system equipped with a Gatan MONO CL4 components under an electron excitation voltage of 5 kV and current of 0.4 nA at room temperature. The μ-PL measurements were performed using a Horiba LabRAM system equipped with confocal optics, a diode-pumped solid-state (DPSS) 532 nm laser and a liquid-nitrogen-cooled array InGaAs detector. The on-sample illuminated spot size is ~ 1.2 μm in diameter and the on-sample power density is 1.6×10^{-5} W/μm^2, achieved with a 50x objective lens (numerical aperture of 0.55). The spectral response of the entire system was determined with a calibrated halogen-tungsten light sources. The electrical properties of the single NW LEDs were characterized by electron beam induced current (EBIC), current-voltage (I-V) and EL measurements. The EBIC was carried out within a FEI Helios 600 Nanolab FIB system with a current of 0.34 nA and an accelerating voltage of 12 kV. The I-V measurements were performed using a Keysight B2902A source and measurement unit.

1
2
3
4
5
6
7
8
9
10
11
12
13
14
15
16
17
18
19
20
21
22
23
24
25
26
27
28
29
30
31
32
33
34
35
36
37
38
39
40
41
42
43
44
45
46
47
48
49
50
51
52
53
54
55
56
57
58
59
60

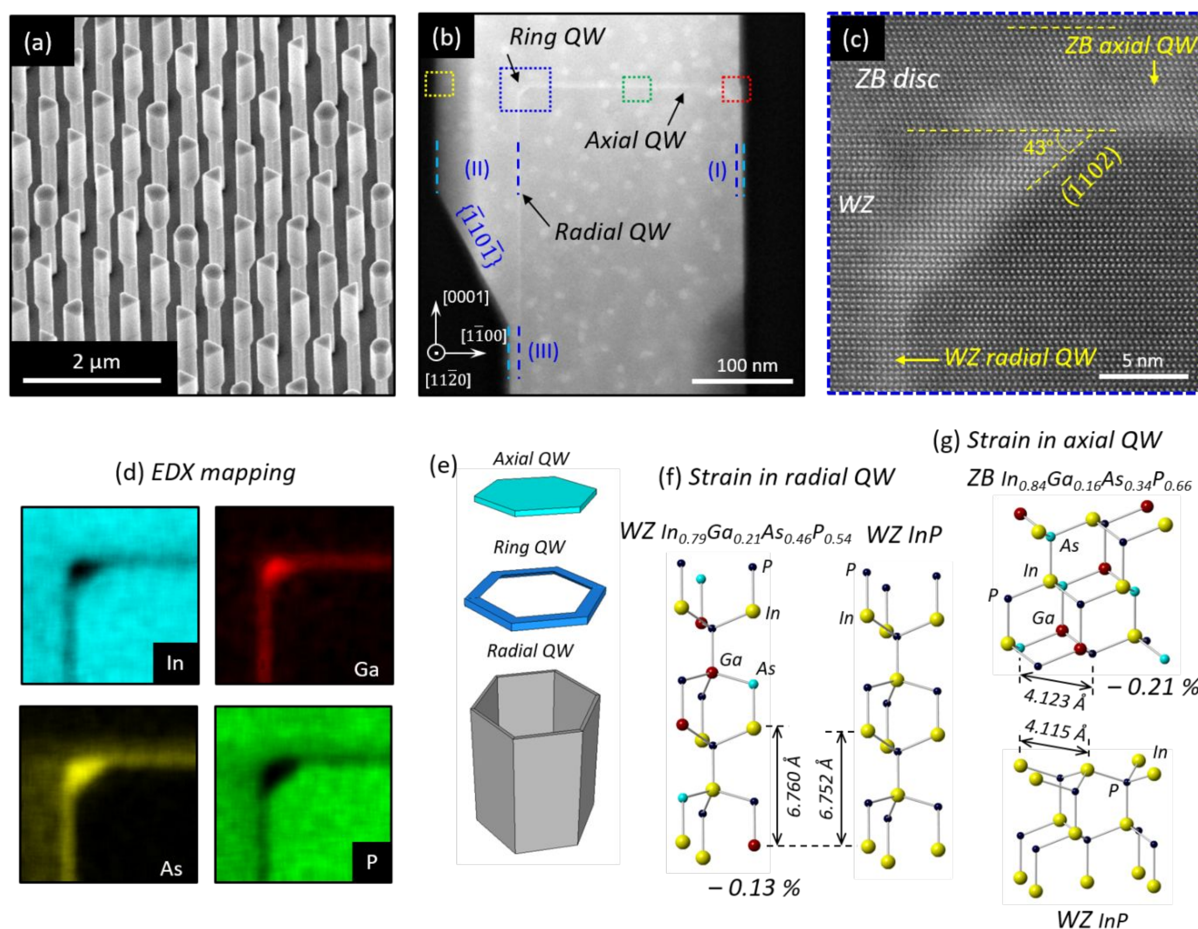

Figure 1. (a) SEM images at 30° tilted view of a single QW NW array grown by SAE-MOCVD technique. (b) AC-STEM image taken along [110] or $[11\bar{2}0]$ zone axis from the QW region. The axial, annular and radial QW are highlighted with black arrows. The

1 2 3 4 5 6 7 8 9 10 11 12 13 14 15 16 17 18 19 20 21 22 23 24 25 26 27 28 29 30 31 32 33 34 35 36 37 38 39 40 41 42 43 44 45 46 47 48 49 50 51 52 53 54 55 56 57 58 59 60

inclined $\{\bar{1}10\bar{1}\}$ facet is marked. The blue dashed lines with (I), (II) and (III) show the n-InP shell thicknesses on each facet. (c) High-resolution AC-STEM image acquired from the blue rectangular area in (b). (d) EDX element mapping images. (e) Schematics of each QW component. (f-g) Strain in the radial (f) and axial (g) QW.

The 30° tilted scanning electron microscopy (SEM) image of the as-grown single QW-NW array is presented in Figure 1a. In agreement with our previous report,[37] the NWs with a single QW have diverse horizontal cross-sectional shapes such as triangles with {112} facets, nonagons and 30° rotated hexagons, all with inclined facets in the middle of the NWs along the growth direction, caused by three-fold symmetric radial growth evolution induced by the insertion of a zinc blende (ZB) InGaAs disc. The microstructural analysis was carried out by AC-STEM on NWs prepared by focused ion beam (FIB)-cross sectioning along the (110) or $(11\bar{2}0)$ plane in a vertical direction (see Figure S2 a in Supporting Information). Figure 1b shows a low magnification AC-STEM image taken along [110] or $[11\bar{2}0]$ zone axis from the QW region. The thin bright region due to arsenic-

rich Z contrast indicates the formation of the single QW in both axial and radial direction around the p-InP base. In Figure 1b, a solely inclined $\{1\bar{1}0\bar{1}\}$ facet with an angle of ~ 28° with respect to the growth direction can also be clearly identified. Figure 1c is the high-resolution AC-STEM image from the blue rectangular box defined in Figure 1b, showing a beveled $(\bar{1}102)$ facet at the corner of the top of p-InP base. From the AC-STEM image, it is confirmed that the truncated facets on both sides of the NW are filled with the subsequently grown WZ QW, indicating that these truncated corner QWs are the cross-section of a continuous hexagonal QW ring. We note that the axial QW is grown in ZB structure on the (0001) plane of the WZ p-InP base while the radial QW is grown in WZ structure on the lateral $\{1\bar{1}00\}$ planes of the WZ p-InP base. All the above observations are consistent with our previously reported 5-InGaAs/InP QW-NW growth study,[37] which finds that the axial QW-induced ZB disc drives the facet evolution from hexagon to various shapes (more detailed results and discussion, see Figure S2 in Supporting Information). Note that the growth on {112}B facet is significantly slower than that on {112}A,[37] resulting in the extremely thin n-InP shell (~ 10 nm) on {112}B side (see (I) in Figure 1b and S2 a). In contrast, on {112}A side, a sufficiently thick n-InP shell (> 70 nm, see (II) in Figure 1b

1
2
3
4
5
6
7
8
9
10
11
12
13
14
15
16
17
18
19
20
21
22
23
24
25
26
27
28
29
30
31
32
33
34
35
36
37
38
39
40
41
42
43
44
45
46
47
48
49
50
51
52
53
54
55
56
57
58
59
60

and S2 a) is grown above the inclined $\{1\bar{1}0\bar{1}\}$ facet and again the n-InP shell becomes thin up to ~ 10nm at the end point of $\{1\bar{1}0\bar{1}\}$ facet (Figure 1b (III)). This is an important feature for understanding the electrical properties of the single NW LED and will be discussed later. It is worth noting that it is possible to further stabilize the lateral facet to realize a more uniform NW morphology. In our previous work,[37] we revealed that the triangular cross-sectional shape has the highest facet formation energy and the 30° rotated hexagons has the lowest one. By changing the growth conditions, we were able to achieve high yield of triangular NWs with no inclined lateral facet. Further study is underway which is beyond the scope of this work and will be reported in the future.

Quantitative analyses of the QW chemical compositions were performed by energy dispersive X-ray spectroscopy (EDX) and the results are presented in Figure 1d (element mapping) and Figure S3 b-d (line-scan). Figure 1d exhibits element mapping images detected from the blue rectangular box in Figure 1b. The images clearly show that the QW region is gallium and arsenic rich with less indium and phosphorous, indicating the incorporation of phosphorous to form an InGaAsP QW due to the arsenic-phosphorous interdiffusion.[39, 40] It is also worth noting that at the corner of the axial and radial QW, a small region with different (higher) gallium and arsenic concentration has been formed,

1
2
3
4
5
6
7
8
9
10
11
12
13
14
15
16
17
18
19
20
21
22
23
24
25
26
27
28
29
30
31
32
33
34
35
36
37
38
39
40
41
42
43
44
45
46
47
48
49
50
51
52
53
54
55
56
57
58
59
60

suggesting the formation of a QW ring structure intersecting the axial and radial QWs, as schematically illustrated in Figure 1e. Here, we note that more arsenic is only observed along the InP lateral shell, indicating the arsenic atoms contained in the QW diffuse out selectively along $\langle 1\bar{1}00 \rangle$ direction. For a thorough investigation of the QW composition, EDX line-scans were carried out across the radial, ring (corner) and axial QW, respectively, with quantitative analysis of their corresponding chemical compositions, as presented in Figure S3 in Supporting Information. As discussed in our previous report,[37] the beveled $\{\bar{1}102\}$ facet at the top corner of the InP base is first filled with the laterally grown QW in WZ phase suggesting that more gallium and arsenic atoms are incorporated during this first lateral growth of the QW. Subsequently, the radial and axial QW are grown independently in different phases and, leading to QWs with different composition and thickness. The radial QW is thinner (~ 6 nm) with higher gallium and arsenic composition whereas the axial QW is thicker (~ 9 nm) with lower gallium and arsenic composition, implying that different surface energy in ZB and WZ phase results in different QW growth rate with different chemical compositions. Therefore, as shown schematically in Figure 1e, the single QW within the NW can be divided into three components with different

compositions and thicknesses. At the positions containing the highest gallium and arsenic contents in the center of each radial, ring, and axial QW, the chemical compositions are $In_{0.79}Ga_{0.21}As_{0.46}P_{0.54}$, $In_{0.58}Ga_{0.42}As_{0.72}P_{0.28}$, and $In_{0.84}Ga_{0.16}As_{0.34}P_{0.66}$, respectively (see Figure S3 in Supporting Information for detail), and these positions are expected to have the maximum strains with respect to the InP barrier. These compositions can be expressed as having the chemical composition of $(InP)_{0.54}(GaAs)_{0.21}(InAs)_{0.25}$ (radial), $(InP)_{0.28}(GaAs)_{0.42}(InAs)_{0.3}$ (ring) and $(InP)_{0.66}(GaAs)_{0.16}(InAs)_{0.18}$ (axial), respectively. Based on the lattice parameters reported by Panse *et al.*,[41] the estimated lattice constant 'c' assuming a proportionality ratio determined for WZ radial and ring QW can be derived to be 6.760 and 6.721 Å, respectively. Likewise, the lattice constant 'a' for the ZB axial QW is estimated to be 4.123 Å, as specified in Figure 1f and g. Consequently, the maximum strain applied to the radial, ring and axial QW interfaces due to the different lattice constant are calculated to be – 0.13 %, + 0.45 %, and – 0.21 %, respectively. This suggests that the ring QW with higher gallium and arsenic content is under a tensile strain whereas the radial and axial QW is subject to very little compressive strain.

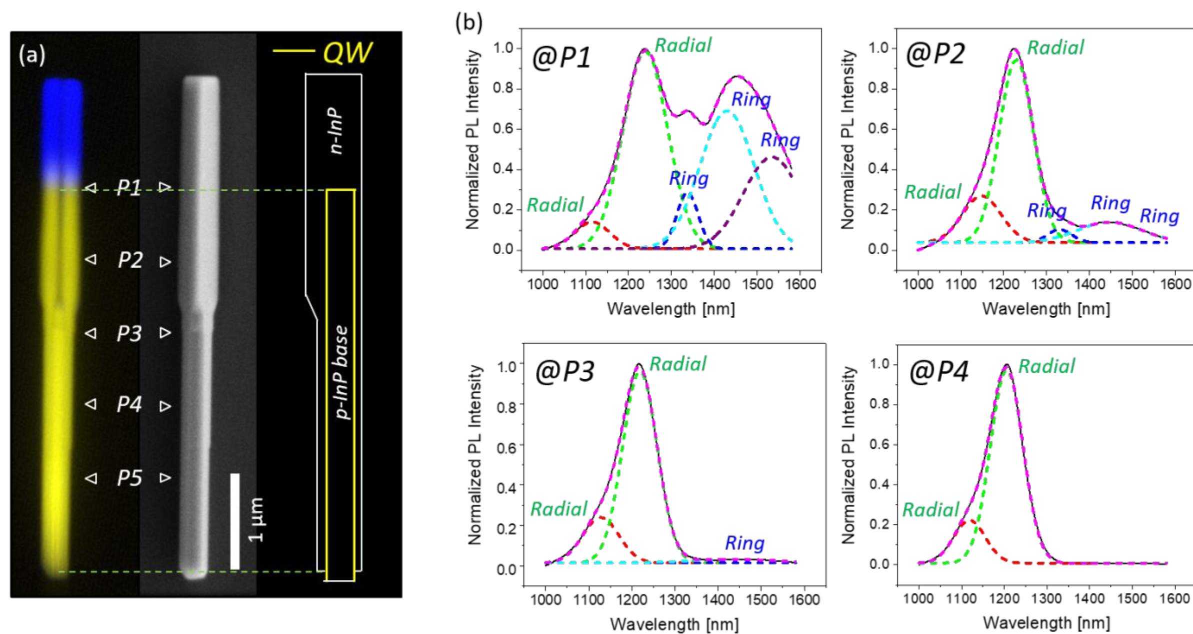

Figure 2. (a) Panchromatic CL image from a single QW NW laid on a Si substrate (left), its corresponding SEM image (middle) and a drawing of the estimated QW location (right). The blue and yellow regions are measured with Si CCD and InGaAs detector, respectively, representing the InP and QW region. The CL and SEM images were taken along the $[1\bar{1}00]$ direction and the schematic was drawn based on the STEM image in Figure 1b which was taken along the $[11\bar{2}0]$ direction. (b) Micro-PL spectra detected from P1 to P4 marked in (a), respectively. P5 is almost identical to P4.

The optical properties of as-grown single QW-NWs were characterized by cathodoluminescence (CL) and micro-photoluminescence (μ-PL) spectroscopy. Figure 2a left shows the CL panchromatic image acquired from a single QW-NW laid on a Si substrate. The blue and yellow regions are the panchromatic images measured with Si CCD (wavelength coverage of < 1 μm) and InGaAs (wavelength coverage of 1 – 1.6 μm) detector, respectively, representing the InP and QW region. As estimated in conjunction with the AC-STEM image in Figure 1b, the blue region with CL wavelengths below 1 μm was detected from the top n-InP segment without the QW layer; whereas the yellow region with CL wavelengths between 1 to 1.6 μm, as originated from the QW, was detected below the axial QW layer, suggesting that the entire p-InP base is covered by the radial QW as depicted in Figure 2a right. It is observed that the CL intensity detected above the inclined $\{1\bar{1}0\bar{1}\}$ facets (above P3) is slightly lower compared to that in the region below the facets. This is related to the penetration depth and angle of incident electrons as a result of the QW-NW morphology. Due to the optical limitation in our CL system which is optimized for visible light, μ-PL was instead used to investigate the spectral map of the NWs.

μ-PL spectra were acquired from different locations on the NW at room temperature. The μ-PL spectra from position 1 to 4 (P1 to P4) are presented in Figure 2b. It is found that the spectrum from P1 is well fitted with a combination of five different Gaussian peaks with wavelengths of approximately 1.1, 1.24, 1.34, 1.43 and 1.54 μm respectively. These peaks can be attributed to different emission from the radial and ring QW. The relatively large full width at half maximum (FWHM) of the luminescence spectrum (around 100 ~ 150 nm) is due to the variation in the QW thickness and composition depending on their facets and locations (see Figure S4a in Supporting Information). It is notable that the peak intensities at ~ 1.34, 1.43 and 1.54 μm abruptly decrease at P2 and are not observed from below P3; while the peaks at ~ 1.1, 1.24 μm are constantly observed from P1 to P5. Considering that the only possible source of luminescence in P3, P4 and P5 is the radial QW, the two peaks with shortest wavelengths are most likely a result of recombination in the radial QW. The main radial QW wavelength peak shows a blue-shift from P1 to P5, indicating the composition and thickness variation along the NW (see Figure S4 a in Supporting Information). Based on the selection rules in a QW, $\Delta n = 0$, we ascribe the two transitions to the first conduction sub-band and the first heavy hole sub-band (c1-hh1),

1 2 3 4 5 6 7 8 9 10 11 12 13 14 15 16 17 18 19 20 21 22 23 24 25 26 27 28 29 30 31 32 33 34 35 36 37 38 39 40 41 42 43 44 45 46 47 48 49 50 51 52 53 54 55 56 57 58 59 60

the second conduction sub-band and the second heavy hole sub-band (c2-hh2), respectively (see Figure S4 b and c in Supporting Information). Here, the transitions between the conduction sub-bands and the light hole sub-bands are not considered because a very small transition between the heavy hole and light hole band is expected due to weak strains in all QW components.

Despite that it is clear that the long wavelengths originate from either the ring or axial QW, it is challenging to determine the luminescence wavelength peaks of axial and ring QW directly from their chemical compositions for two reasons. Firstly, the diffused interfaces between the QW and barrier changes the quantum confinement. Secondly, the bandgap energies of the WZ quaternary alloys have not been reported in the literature. According to Yamazoe *et al.*, the band gap energy of ZB $In_{1-x}Ga_xAs_yP_{1-y}$ quaternary alloy lattice-matched to InP is given as $\mathrm{E}_g = 1.35 - 0.738 \cdot y + 0.138 \cdot y^2$ at room temperature.[42] From this equation, the bandgap energies of the ring and axial QW are calculated to be ~ 0.89 and ~ 1.115 eV, which correspond to the wavelengths of ~ 1.39 and ~ 1.11 μm, respectively, assuming no quantum confinement effect. Also from the empirical equation it can be noted that more arsenic lead to a lower bandgap energy and a longer emission

wavelength. Moreover, the ring QW is much thicker than the axial QW, suggesting less quantum confinement effect. From these, we suggest that the three long wavelength peaks at ~ 1.34, 1.43 and 1.54 μm are most likely due to the ring QW with higher gallium and arsenic compositions. Similarly, the luminescence wavelength peaks from the axial QW are expected to be around 1.1 ~ 1.2 μm considering its composition. In fact, in contrast to the radial and ring QW, the main luminescent direction of the axial QW is perpendicular to the detection angle such that the light is hardly detected due to angle limitation of the μ-PL detection system. Moreover, for the light emitted from the axial QW within the detection angle, it is likely to be reabsorbed by the surrounding ring QW with lower bandgap, which could lead to an increased optical injection level of the ring QW, and thus an increase of luminescence intensity despite its small volume.

1 2 3 4 5 6 7 8 9 10 11 12 13 14 15 16 17 18 19 20 21 22 23 24 25 26 27 28 29 30 31 32 33 34 35 36 37 38 39 40 41 42 43 44 45 46 47 48 49 50 51 52 53 54 55 56 57 58 59 60

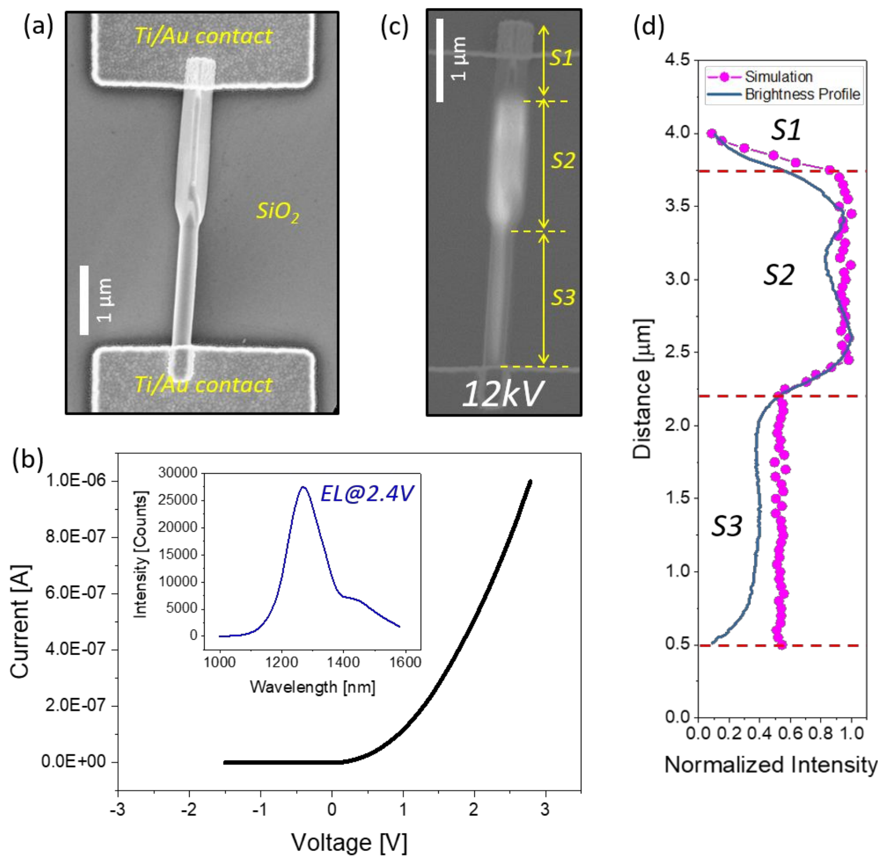

Figure 3. (a) SEM image of the fabricated single NW LED. (b) I-V curve measured with the fabricated single NW LED (black solid line). Inset panel is the EL spectrum measured at 2.4 V. (c) EBIC signal image acquired under an accelerating voltage of 12 kV overlaid on its corresponding SEM image. (d) EBIC profile along the center of the NW (navy blue solid line) and simulated EBIC profile (magenta dots).

Figure 3a displays the SEM image of a fabricated single NW LED device (see Figure S1 for fabrication process images). Figure 3b shows a typical diode I-V curve measured from a single NW LED, indicating the formation of a p-n junction. The formation of a p-n junction was also confirmed by EBIC measurements with the fabricated device and presented in Figure 3c. The EBIC image was measured under an accelerating voltage of 12 kV, clearly showing three individual sections with different brightness, which correspond to the sole n-InP segment (S1), the thick n-InP shell/QW/p-InP base (S2) and the thin n-InP shell/QW/p-InP (S3), respectively. At the boundary of S1 and S2, there is a mixture of axial and radial junction, contributing to the EBIC signal. The extended EBIC signal up to the bottom of the NW clearly shows the presence of fully covered radial junction. It is worth noting that the boundary between S2 and S3 is determined by the inclined $\{\bar{1}10\bar{1}\}$ facet. The EBIC signal is contributed by the current density, $J_{tot} = J_{scr.net} + J_n + J_p$, where, $J_{scr.net}$, J_n and J_p are the current density due to the drifting electrons and holes in space charge region (SCR) generated by the electron-beam (e-beam), diffusing electrons (J_n) and holes (J_p) generated by the e-beam within the electron diffusion length (L_n) in p-region and the hole diffusion length (L_p) in n-region, respectively. $J_{scr.net}$, again, can be written

1 2 3 4 5 6 7 8 9 10 11 12 13 14 15 16 17 18 19 20 21 22 23 24 25 26 27 28 29 30 31 32 33 34 35 36 37 38 39 40 41 42 43 44 45 46 47 48 49 50 51 52 53 54 55 56 57 58 59 60

as, $J_{scr.net} = J_{gen} - J_{rec}$, where, J_{gen} and J_{rec} are the generation and recombination current density in the SCR containing the QW. The penetration depth of 90% of incident electrons into the NW was estimated to be ~ 300 nm at 12 kV by 2D Casino simulation[43] using Monte Carlo method, indicating that the incident electrons interact with the whole volume of NW. Hence, the valid interaction depth contributing to the EBIC signal will be determined in the range of $W + L_n + L_p$ and given as,[44]

$$W = X_p + X_n = \sqrt{\frac{2\varepsilon}{q}\left(\frac{1}{N_A} + \frac{1}{N_D}\right)(V_{bi} - V_{app})} \quad (1)$$

$$V_{bi} = \frac{kT}{q} ln\left(\frac{N_A N_D}{n_i^2}\right) \quad (2)$$

where, W, X_p and X_n are the total SCR width, the SCR width in p-region, and n-region, respectively. For $n_i = 1.2 \times 10^8 cm^{-3}$ at 300 K,[45] $N_A \sim 5.0 \times 10^{17} cm^{-3}$, $N_D \sim 2.5 \times 10^{18}$ cm^{-3}, and applied voltage, $V_{app} = 0$ (unbiased EBIC), the built-in voltage and the total SCR width are calculated to be approximately 1.19 V and 63 nm, respectively. Here, N_D $\sim 2.5 \times 10^{18} cm^{-3}$ was derived by power dependent PL measurements.[46] Unlike the n-

1
2
3
4
5
6
7
8
9
10
11
12
13
14
15
16
17
18
19
20
21
22
23
24
25
26
27
28
29
30
31
32
33
34
35
36
37
38
39
40
41
42
43
44
45
46
47
48
49
50
51
52
53
54
55
56
57
58
59
60

doping case, determining the p-doping concentration remains challenging. Based on our previous work,[47] the current growth condition, and Comsol simulation of the EBIC profile (see Figure S5 in Supporting Information for details) in Figure 3d, an $N_A \sim 5.0 \times 10^{17} cm^{-3}$ is assumed. According to a report,[48] L_n for the p-doped InP NW of $5 \times 10^{18} cm^{-3}$ and L_p for the n-doped InP NW of $1 \times 10^{19} cm^{-3}$ were estimated to be 160 and 65 nm, respectively. Considering lower doping levels for both p- and n-InP in this work, L_n and L_p are estimated to be over ~ 200 and 100 nm, respectively. This indicates that the minority carriers created in any location of the NW junction area contribute to J_{tot}, resulting in the different EBIC intensity contrast arising from S2 and S3 region due to their different horizontal cross-sectional area. This is in good agreement with the EBIC profile shown with the solid line in Figure 3d, which was also confirmed by the 2D p-n junction simulation with the Comsol software (see Figure S5 in Supporting Information for details) and overlaid on the experimental EBIC profile in Figure 3d.

1
2
3
4
5
6
7
8
9
10
11
12
13
14
15
16
17
18
19
20
21
22
23
24
25
26
27
28
29
30
31
32
33
34
35
36
37
38
39
40
41
42
43
44
45
46
47
48
49
50
51
52
53
54
55
56
57
58
59
60

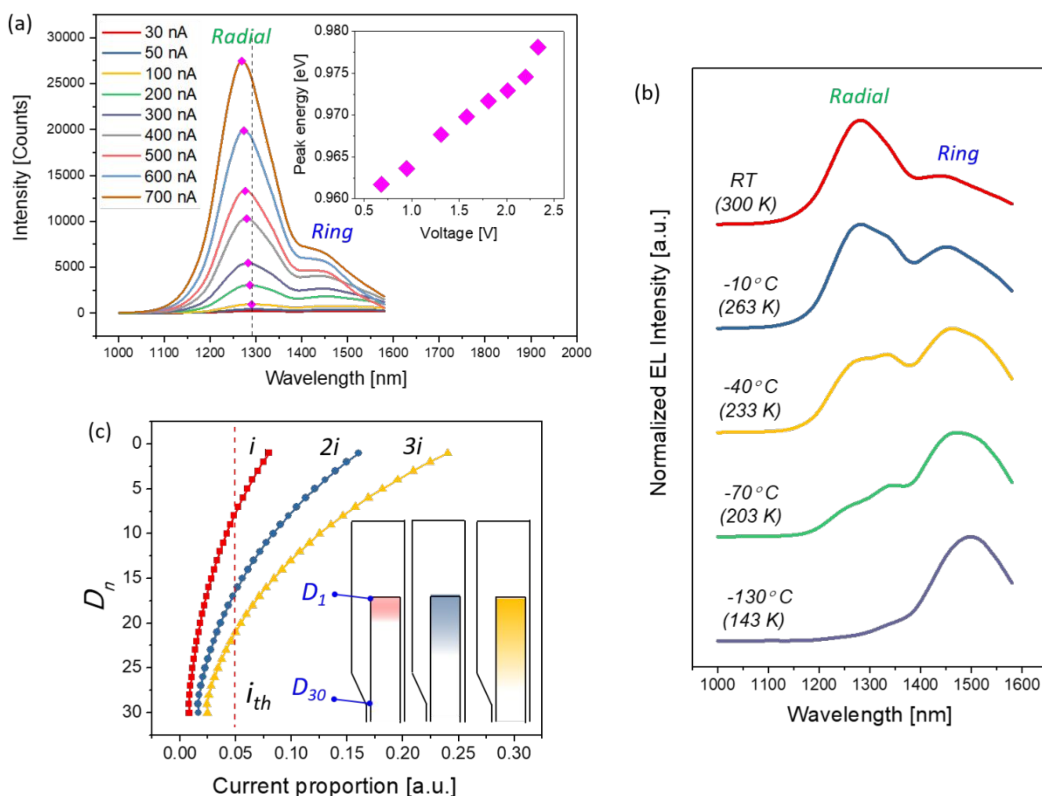

Figure 4. (a) EL spectra with increasing current injection at room temperature. Inset shows a blue shift of the radial QW peak with increased forward bias. (b) Normalized EL spectra measured at room temperature, -10°C, -40 °C, -70 °C and -130 °C, respectively. (c) Current proportion distributed to each unit diode with increasing current *i*, *2i* and *3i*. An arbitrary threshold current level (i_{th}) at room temperature is marked with red dashed line. Inset in (c) illustrates the activated radial QW region where the higher current than threshold current flows in case of each current level.

Figure 4a shows EL spectra from the single NW LED with increasing current injection level at room temperature. The integrated intensity increases with current level as typical LEDs. In Figure 4a, it is observed that the intensity of wavelength peak from the radial QW (shorter wavelength region) significantly increases with increasing current as compared to that from the ring QW (longer wavelength region). These are clearly shown with the normalized EL spectra in Figure S6 (in Supporting Information). With a low current of 50 nA, it is shown that the EL intensity from the ring QW is comparable to that from the radial QW. However, as the injection current increases, the intensity from the radial QW increases over that of the ring QW. In Figure 4a inset, the main peak emission from the radial QW is observed to show a blue shift, which is likely due to the QW thickness and composition variation along the NW (see Figure S4 a in Supporting Information). In Figure 4a, the FWHM of EL (~ 150 nm) is observed to be slightly larger than that of the PL, due to contribution from the ring QW, as can be seen in Figure S6.

To investigate the temperature dependence of the device, the EL spectra were measured at the bias of 2.0 V from room temperature to -130 °C and presented in Figure 4b. In this Figure, it is clearly observed that the intensity of shorter wavelength peaks

abruptly decreases with decreasing temperature (see Figure S7 in Supporting Information for detail). This wavelength spectrum variation clearly indicates that, as temperature decreases, the radiative recombination in the radial QW dramatically decreases and, in the ring QW, more radiative recombination occurs by electrons and holes occupying the lowest energy state.

Simulations on current distribution in InGaN/GaN core-shell NWs have been investigated by several groups.[49-51] Especially, Tchernycheva *et al*. successfully explained the EL spectral behaviors of their InGaN/GaN core-shell single NW LEDs with current injections by introducing a simple electrical model.[20] To understand the EL spectra evolution as a function of injection power and measurement temperature, we qualitatively develop an equivalent circuit model based on the distinctive geometrical and electrical structure of our QW-NW. In this model, the radial p-n junction regions above the inclined facet were considered as a series of infinitely connected parallel diodes as described in Figure S9 a and the current flowing through these regions were derived by considering the resultant resistance of the equivalent circuit presented in Figure S9 b. (see Figure S8, S9 and S10 in Supporting Information for details on the equivalent circuit model). The

current proportions flowing through each radial diode are presented in Figure 4c, where D_n represents the arranged diodes in parallel from the top of p-InP base (right below the ring QW). The D_1 and D_{30} are defined to be the radial diode located at the boundaries right below the ring QW (between the Section 1a and 2a in Figure S8 b), and right above the inclined facet (between the Section 2a and 3a in Figure S8 b), respectively. Figure 4c clearly shows that the activated region above an arbitrary threshold current level (i_{th}) at room temperature (red dashed line) increases with increasing injection current, indicating that higher current injection induces recombination over larger area from the top of radial QW as depicted with colored areas in Figure 4c inset. Here, the threshold current can be defined to be a minimum current generating more radiative recombination over non-radiative recombination, producing detectable EL. This explains both the evolution of the EL spectra and the blue-shift of the main radial QW EL peak (Figure 4a) with increasing current injection very well. The temperature dependence of the EL spectra can be also well explained by this model. In general, the conductivity of a semiconductor decreases with the decrease of temperature, implying that the current level over the entire NW drops with decreasing temperature at the same applied bias and in other words, recombination becomes

1
2
3 restricted to the area closer to the top of radial QW at lower temperatures. Consequently, this
4
5
6
7 leads to a decrease in the radial QW component of the EL spectra, as shown in Figure 4b.
8
9
10 Simultaneously, due to reduced thermal leakage, more electrons and holes occupy the lowest
11
12
13 state with decreasing temperature, resulting in a decrease of the higher energy transitions
14
15
16
17 and, in turn, an increase of the lowest energy transition in the ring QW (see Figure S10 in
18
19
20 Supporting Information for detail).

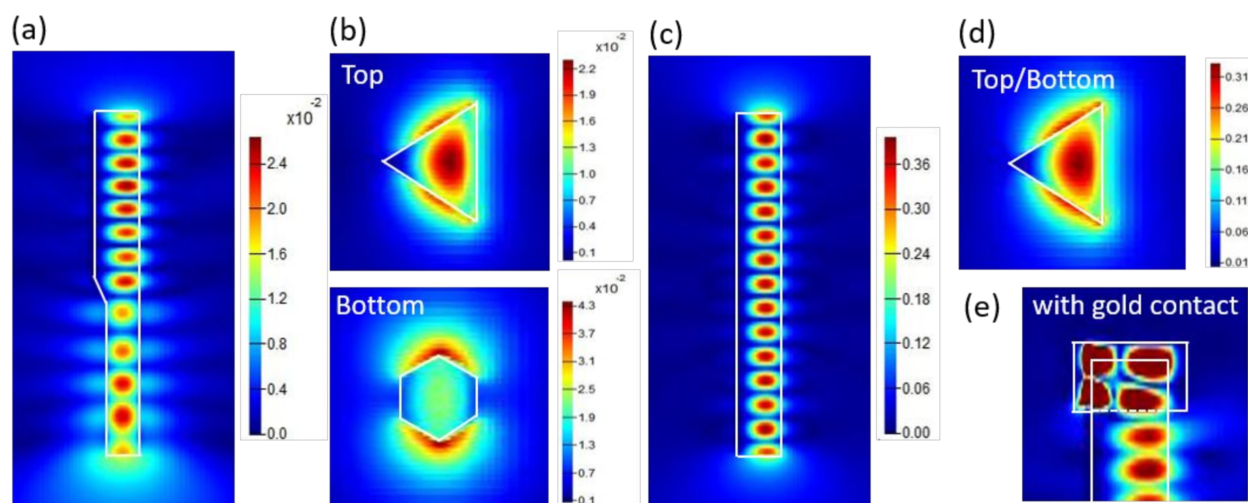

45 Figure 5. Electric-field profiles ($|E|^2$) of the optical mode confined in the NW with inclined
46
47
48
49 facet (a-b) and with no inclined facet (c-d). (a) and (c) show vertical cross-sectional
50
51
52 electric-field profiles and (b) and (d) show horizontal cross-sectional electric-field profiles
53
54
55
56
57
58
59
60

from each NW. (e) shows a vertical cross-sectional electric-field profile from the inclined facet NW with a gold contact. The color scale of (e) is same as that in (a).

Finally, to understand the effect of inclined facet on the light behavior in the single NW LED, the three-dimensional FDTD simulation was performed for two NW cases, one with inclined facet and another with no inclined facet. The NWs (n = 3.2) were designed to have a length of 4.6 μm and diameter of 460 nm. Figure 5 presents the electric-field profiles of the optical mode at ~ 1.27 μm wavelength confined in the NW with inclined facet (a-b) and with no inclined facet (c-d), respectively. The NW with inclined facet consists of two segments, a triangular horizontal cross-section above the inclined facet and a hexagonal horizontal cross-section below the inclined facet whereas the NW with no facet has only triangular horizontal cross-section throughout the NW. Figure 5a clearly shows asymmetric electric-field profile with the inclined facet as a boundary. We note that the intensity of electric-field in the triangular section is higher as compared with the hexagonal section while the NW with no inclined facet shows better confined electric-field

with much higher intensity. This indicates that the optical mode at ~ 1.27 μm is confined much better in the triangular NW. The light extraction efficiency on each side was also obtained. In case of the NW with inclined facet, the light extractions to the top (triangle), bottom (hexagon), and the sides are 13.5, 37.9, and 45.2 %, respectively. In contrast, the light extractions of the NW with no inclined facet to the top, bottom, and the sides are 25.3, 25.3, and 43.8%, respectively. It clearly indicates that almost half of light leaks through the top and bottom facet of NW in both cases. In addition, ~ 1.5 % of more light is extracted through the hexagonal section of the NW with inclined facet. To understand the effect of gold metal contact, the NW with inclined facet was simulated with 100 nm gold contact and presented in Figure 5e. It is found that most of light propagating toward the top and bottom is absorbed by the gold contact, leading to reduced light extraction for the top (triangle), bottom (hexagon), and side to be 0.4, 4, and 37.54%, respectively. In the future a contact metal with a low light absorption coefficient at the desired optical modes has to be chosen to maximize the light extraction.

In conclusion, we demonstrate single NW LEDs based on a single InGaAs/InP QW grown by MOCVD using SAE technique. Through quantitative analyses of the QW

chemical composition, we reveal that the QW is composed of three components with different chemical compositions, radial QW, ring QW and axial QW, leading to multiple-wavelength PL and EL emissions. From EL measurements, it is observed that the proportion of the EL from the radial QW increases with increasing current injection. With decreasing measurement temperature, the EL from the radial QW abruptly decrease and, simultaneously, the lower energy transition in the ring QW becomes predominant. The optoelectrical behavior of the single NW LED can be well understood by interpreting the equivalent circuits in the device which are closely related to the distinctive triangular morphology with the inclined facet of the NW. In addition, through the FDTD simulation, it was revealed that the optical mode at ~1.27 μm is much better confined in the triangular segment of NW thus more light is extracted from the hexagonal segment of our QW-NW LED. A large optical loss through metal contact areas was also found, indicating the significance of contact metal selection to avoid light absorption.

The unique correlation between the geometrical and electrical structure of QW-NW LED revealed by our work directs new pathways on both NW growth and device design to achieve high efficiency InGaAs/InP QW-NW LEDs such as: 1) Shortening the top n-

segment of the NW to reduce the unnecessary resistance; 2) tuning the growth parameters to grow perfect hexagonal InP shell[37] without inclined facets instead of triangular one with inclined facets to secure a large luminescent area with larger shell thickness and non-inclined facet; 3) Using transparent conductive contact to cover a wide area of radial QW as well as increasing doping concentration for both p- and n-segments to increase the overall current injection efficiency; and 4) Choosing an appropriate metal to achieve good Ohmic contacts on both p- and n-side and minimize the optical loss. Finally, the multi-wavelength single NW InGaAs/InP QW LEDs in this work also show great potential for achieving integrated wavelength-selective nanoscale LEDs. For example, by introducing an additional transparent wrap gate around the sidewall of NW, the selectivity of the emitting wavelengths could be precisely controlled, which is a new device concept potentially useful for development of future nanoscale electrically switchable wavelength selector for wavelength division multiplexing systems.

Supporting Information

Section 1: Optical and SEM images of fabricated and wire bonded single NW LED; Section 2: Zinc blende disc in single QW NW; Section 3: EDX line-scan; Section 4: Position and power dependent PL spectra at room temperature; Section 5: Electron beam induced current simulation; Section 6: Normalized EL spectra with different current injection levels; Section 7: Normalized EL spectra at low temperatures; Section 8: Simple equivalent circuit model for the single NW with the distinctive facets.

Acknowledgements

The authors acknowledge the Australian Research Council for financial support. The authors also acknowledge the Australian National Fabrication Facility (ACT node), the Australian Microscopy and Microanalysis Research Facility (ACT node) for facility support. The authors acknowledge Dr. G. Casillas for access to and operation of the AC-STEM instrument (JEOL JEM-ARM200F) in the University of Wollongong Electron Microscopy Centre. The authors also would like to thank Prof. D. Macdonald for access to the μ-PL facility at the Research School of Electrical, Energy and Materials Engineering, the

Australian National University. I. Yang acknowledges the support of AGRTP scholarship from the Australian Government. H. T. Nguyen acknowledges the support of a fellowship from the Australian Centre for Advanced Photovoltaics.

References

1. Vlasov, Y. A. *IEEE Communications Magazine* **2012,** 50, (2), 67-72.
2. Cheng, Z.; Ríos, C.; Pernice, W. H.; Wright, C. D.; Bhaskaran, H. *Sci. Adv* **2017,** 3, (9), e1700160.
3. Pérez, D.; Gasulla, I.; Crudgington, L.; Thomson, D. J.; Khokhar, A. Z.; Li, K.; Cao, W.; Mashanovich, G. Z.; Capmany, J. *Nat. Commun.* **2017,** 8, (1), 636.
4. Lim, A. E.-J.; Song, J.; Fang, Q.; Li, C.; Tu, X.; Duan, N.; Chen, K. K.; Tern, R. P.-C.; Liow, T.-Y. *IEEE J. Sel. Top. Quantum Electron.* **2014,** 20, (4), 405-416.
5. Wang, Z.; Abbasi, A.; Dave, U.; Groote, A.; Kumari, S.; Kunert, B.; Merckling, C.; Pantouvaki, M.; Shi, Y.; Tian, B. *Laser Photonics Rev.* **2017,** 11, (4), 1700063.

6. Chen, R.; Tran, T.-T. D.; Ng, K. W.; Ko, W. S.; Chuang, L. C.; Sedgwick, F. G.; Chang-Hasnain, C. *Nat. Photonics* **2011,** 5, (3), 170.

7. Zubia, D.; Hersee, S. *J. Appl. Phys* **1999,** 85, (9), 6492-6496.

8. Luryi, S.; Suhir, E. *Appl. Phys. Lett.* **1986,** 49, (3), 140-142.

9. Li, Z.; Tan, H. H.; Jagadish, C.; Fu, L. *Adv. Mater. Technol.* **2018,** 3, (9), 1800005.

10. Bar-Sadan, M.; Barthel, J.; Shtrikman, H.; Houben, L. *Nano Lett.* **2012,** 12, (5), 2352-2356.

11. Breuer, S.; Pfüller, C.; Flissikowski, T.; Brandt, O.; Grahn, H. T.; Geelhaar, L.; Riechert, H. *Nano Lett.* **2011,** 11, (3), 1276-1279.

12. Lang, D.; Grimmeiss, H.; Meijer, E.; Jaros, M. *Phys. Rev. B* **1980,** 22, (8), 3917.

13. Tatebayashi, J.; Kako, S.; Ho, J.; Ota, Y.; Iwamoto, S.; Arakawa, Y. *Nat. Photonics* **2015,** 9, (8), 501-505.

14. Gao, Q.; Saxena, D.; Wang, F.; Fu, L.; Mokkapati, S.; Guo, Y.; Li, L.; Wong-Leung, J.; Caroff, P.; Tan, H. H.; Jagadish, C. *Nano Lett.* **2014,** 14, (9), 5206-5211.

15. Schuster, F.; Kapraun, J.; Malheiros-Silveira, G. N.; Deshpande, S.; Chang-Hasnain, C. J. *Nano Lett.* **2017,** 17, (4), 2697-2702.

16. Deshpande, S.; Bhattacharya, I.; Malheiros-Silveira, G.; Ng, K. W.; Schuster, F.; Mantei, W.; Cook, K.; Chang-Hasnain, C. *ACS Photonics* **2017,** 4, (3), 695-702.

17. Tomioka, K.; Motohisa, J.; Hara, S.; Hiruma, K.; Fukui, T. *Nano Lett.* **2010,** 10, (5), 1639-1644.

18. Berg, A.; Yazdi, S.; Nowzari, A.; Storm, K.; Jain, V.; Vainorius, N.; Samuelson, L.; Wagner, J. B.; Borgström, M. T. *Nano Lett.* **2015,** 16, (1), 656-662.

19. Hersee, S. D.; Fairchild, M.; Rishinaramangalam, A. K.; Ferdous, M. S.; Zhang, L.; Varangis, P. M.; Swartzentruber, B. S.; Talin, A. A. *Electron. Lett.* **2009,** 45, (1), 75-76.

20. Tchernycheva, M.; Lavenus, P.; Zhang, H.; Babichev, A. V.; Jacopin, G.; Shahmohammadi, M.; Julien, F. H.; Ciechonski, R.; Vescovi, G.; Kryliouk, O. *Nano Lett.* **2014,** 14, (5), 2456-2465.

21. Tchernycheva, M.; Messanvi, A.; de Luna Bugallo, A.; Jacopin, G.; Lavenus, P.; Rigutti, L.; Zhang, H.; Halioua, Y.; Julien, F. H.; Eymery, J.; Durand, C. *Nano Lett.* **2014,** 14, (6), 3515-3520.

22. Musolino, M.; Tahraoui, A.; Fernández-Garrido, S.; Brandt, O.; Trampert, A.; Geelhaar, L.; Riechert, H. *Nanotechnology* **2015,** 26, (8), 085605.

23. Thijs, P. J. A.; Tiemeijer, L. F.; Kuindersma, P. I.; Binsma, J. J. M.; Dongen, T. V. *IEEE J. Quantum Electron.* **1991,** 27, (6), 1426-1439.

24. Fonseka, H.; Ameruddin, A.; Caroff, P.; Tedeschi, D.; De Luca, M.; Mura, F.; Guo, Y.; Lysevych, M.; Wang, F.; Tan, H. *Nanoscale* **2017,** 9, (36), 13554-13562.

25. Lu, F.; Bhattacharya, I.; Sun, H.; Tran, T.-T. D.; Ng, K. W.; Malheiros-Silveira, G. N.; Chang-Hasnain, C. *Optica* **2017,** 4, (7), 717-723.

26. Malheiros-Silveira, G. N.; Bhattacharya, I.; Deshpande, S. V.; Skuridina, D.; Lu, F.; Chang-Hasnain, C. J. *Opt. Express* **2017,** 25, (1), 271-277.

1
2
3
4
5
6
7
8
9
10
11
12
13
14
15
16
17
18
19
20
21
22
23
24
25
26
27
28
29
30
31
32
33
34
35
36
37
38
39
40
41
42
43
44
45
46
47
48
49
50
51
52
53
54
55
56
57
58
59
60

27. Gradečak, S.; Qian, F.; Li, Y.; Park, H.-G.; Lieber, C. M. *Appl. Phys. Lett.* **2005,** 87, (17), 173111.

28. Röder, R.; Wille, M.; Geburt, S.; Rensberg, J.; Zhang, M.; Lu, J. G.; Capasso, F.; Buschlinger, R.; Peschel, U.; Ronning, C. *Nano Lett.* **2013,** 13, (8), 3602-3606.

29. Johnson, J. C.; Yan, H.; Schaller, R. D.; Haber, L. H.; Saykally, R. J.; Yang, P. *J. Phys. Chem. B* **2001,** 105, (46), 11387-11390.

30. Takiguchi, M.; Zhang, G.; Sasaki, S.; Nozaki, K.; Chen, E.; Tateno, K.; Tawara, T.; Shinya, A.; Gotoh, H.; Notomi, M. *Appl. Phys. Lett.* **2018,** 112, (25), 251106.

31. Li, Z.; Yuan, X.; Fu, L.; Peng, K.; Wang, F.; Fu, X.; Caroff, P.; White, T. P.; Tan, H. H.; Jagadish, C. *Nanotechnology* **2015,** 26, (44), 445202.

32. Dai, X.; Zhang, S.; Wang, Z.; Adamo, G.; Liu, H.; Huang, Y.; Couteau, C.; Soci, C. *Nano Lett.* **2014,** 14, (5), 2688-2693.

33. Tian, B.; Kempa, T. J.; Lieber, C. M. *Chem. Soc. Rev.* **2009,** 38, (1), 16-24.

34. Zhong, Z.; Li, Z.; Gao, Q.; Li, Z.; Peng, K.; Li, L.; Mokkapati, S.; Vora, K.; Wu, J.; Zhang, G. *Nano Energy* **2016,** 28, 106-114.

35. Kelzenberg, M. D.; Turner-Evans, D. B.; Kayes, B. M.; Filler, M. A.; Putnam, M. C.; Lewis, N. S.; Atwater, H. A. *Nano Lett.* **2008,** 8, (2), 710-714.

36. Krogstrup, P.; Jørgensen, H. I.; Heiss, M.; Demichel, O.; Holm, J. V.; Aagesen, M.; Nygard, J.; i Morral, A. F. *Nat. Photonics* **2013,** 7, (4), 306.

37. Yang, I.; Zhang, X.; Zheng, C.; Gao, Q.; Li, Z.; Li, L.; Lockrey, M. N.; Nguyen, H.; Caroff, P.; Etheridge, J.; Tan, H. H.; Jagadish, C.; Wong-Leung, J.; Fu, L. *ACS Nano* **2018,** 12, (10), 10374-10382.

38. Karimi, M.; Heurlin, M.; Limpert, S.; Jain, V.; Zeng, X.; Geijselaers, I.; Nowzari, A.; Fu, Y.; Samuelson, L.; Linke, H. *Nano Lett.* **2017,** 18, 365-372.

39. Yamakawa, I.; Oga, R.; Fujiwara, Y.; Takeda, Y.; Nakamura, A. *Appl. Phys. Lett.* **2004,** 84, (22), 4436-4438.

1
2
3
4
5
6
7
8
9
10
11
12
13
14
15
16
17
18
19
20
21
22
23
24
25
26
27
28
29
30
31
32
33
34
35
36
37
38
39
40
41
42
43
44
45
46
47
48
49
50
51
52
53
54
55
56
57
58
59
60

40. Sudo, S.; Nakano, Y.; Sugiyama, M.; Shimogaki, Y.; Komiyama, H.; Tada, K. *Thin Solid Films* **1998,** 313, 604-608.

41. Panse, C.; Kriegner, D.; Bechstedt, F. *Phys. Rev. B* **2011,** 84, (7), 075217.

42. Yamazoe, Y.; Nishino, T.; Hamakawa, Y.; Kariya, T. *Jpn. J. Appl. Phys.* **1980,** 19, (8), 1473.

43. Casino http://www.gel.usherbrooke.ca/casino/

44. Taur, Y.; Ning, T. H., *Fundamentals of modern VLSI devices*. 2013.

45. Ban, D.; Sargent, E.; Dixon-Warren, S. J.; Calder, I.; SpringThorpe, A.; Dworschak, R.; Este, G.; White, J. *Appl. Phys. Lett.* **2002,** 81, (26), 5057-5059.

46. Wang, F.; Gao, Q.; Peng, K.; Li, Z.; Li, Z.; Guo, Y.; Fu, L.; Smith, L. M.; Tan, H. H.; Jagadish, C. *Nano Lett.* **2015,** 15, (5), 3017-3023.

47. Gao, Q.; Li, Z.; Li, L.; Vora, K.; Li, Z.; Alabadla, A.; Wang, F.; Guo, Y.; Peng, K.; Wenas, Y. C. *Prog. Photovolt. Res. Appl.*

48. Wallentin, J.; Wickert, P.; Ek, M.; Gustafsson, A.; Reine Wallenberg, L.; Magnusson, M. H.; Samuelson, L.; Deppert, K.; Borgström, M. T. *Appl. Phys. Lett.* **2011,** 99, (25), 253105.

49. Der Maur, M. A.; Sacconi, F.; Di Carlo, A. *IEEE Trans. Electron Devices* **2013,** 60, (1), 171-177.

50. Li, C.-K.; Yang, H.-C.; Hsu, T.-C.; Shen, Y.-J.; Liu, A.-S.; Wu, Y.-R. *J. Appl. Phys* **2013,** 113, (18), 183104.

51. Mazuir, C.; Schoenfeld, W. V. *J. Nanophotonics* **2007,** 1, (1), 013503.

1
2
3
4
5
6
7
8
9
10
11
12
13
14
15
16
17
18
19
20
21
22
23
24
25
26
27
28
29
30
31
32
33
34
35
36
37
38
39
40
41
42
43
44
45
46
47
48
49
50
51
52
53
54
55
56
57
58
59
60